Diffuse scattering from interface roughness in grazing-incidence x-ray diffraction

S. A. Stepanov,* E. A. Kondrashkina,* M. Schmidbauer, R. Köhler, and J.-U. Pfeiffer
MPG-AG ''Röntgenbeugung,'' Hausvogteiplatz 5-7, Berlin D-10117, Germany

T. Jach
National Institute of Standards and Technology, Gaithersburg, Maryland 20899

A. Yu. Souvorov
European Synchrotron Radiation Facility, Boîte Postale 220, Grenoble Cedex F-38043, France
(Received 12 March 1996)

A theory of x-ray diffuse scattering from interface roughness in grazing-incidence diffraction (GID) is presented. The theory assumes dynamical diffraction of x rays from perfect multilayers with the diffuse scattering from roughness calculated in the distorted-wave Born approximation. This permits the calculation of scattering due to roughness at all points on the diffraction curves, including the vicinity of the Bragg peaks. It is shown that the measurements of diffuse scattering in GID can provide information on atomic ordering at crystal interfaces which is not accessible by usual x-ray specular reflection and nonspecular x-ray scattering. The theory is found to be in good agreement to the two GID experiments carried out with an etched Ge surface and an AlAs/GaAs superlattice at the Cornell High-Energy Synchrotron Source and European Synchrotron Radiation Facility, respectively. In the case of the etched Ge surface, an anti-Yoneda dip in the diffuse scattering pattern at the Bragg peak and two symmetrical shoulders on the Bragg curve wings have been found and explained. In the case of the AlAs/GaAs superlattice, the diffuse scattering has been separated from GID by means of high-resolution measurements. A comparison between diffuse scattering in GID and diffuse scattering in grazing incidence far from the diffraction conditions has shown that the atomic ordering was preserved in the interface roughness, while it was partially destroyed in the surface roughness. [S0163-1829(96)05035-7]

I. INTRODUCTION

The combination of Bragg diffraction and total external reflection (TER) effects in grazing-incidence x-ray diffraction (GID) opens up a wealth of possibilities in the study of thin surface layers of crystals.[1–4] GID has been applied with success to investigations of the surface treatment and surface oxidation of semiconductor wafers,[5,6] to studies of structure transformations during ion implantation,[7–9] and to analysis of strain relaxation in epitaxial layers[1,10,11] and multilayers.[12]

The measurements of diffuse scattering (DS) in GID can provide additional information on crystal lattice defects in surface layers.[13,14] However, along with diffuse scattering caused by lattice defects, strong scattering due to surface and interface roughness can be expected in GID by analogy with x-ray TER studies, since the angle of incidence of the x rays is equally small in both these cases.[15–19] Roughness can also give rise to a change in the diffracted intensities.[20–22] Thus one has to distinguish between the effects of roughness and crystal lattice defects on GID.

The effect of roughness on x-ray Bragg diffraction has not been adequately explored. As shown in Ref. 23, in normal-incidence diffraction geometries the effect is relatively weak. In GID, there are several theoretical predictions[21,22] of a strong effect of roughness on the coherent reflection. However, only a few experimental results[20,15] are known, and they are not in good agreement with the theory. In particular, in Ref. 15 an enhancement of the intensity of the tails of the diffracted beam of GID measured from a rough surface was observed, while in Ref. 21 an attenuation of the tails with an exponent similar to that found by Névot and Croce[24,25] for the tails of x-ray specular reflection curves was predicted.

We have assumed that discrepancies between Refs. 15 and 21 were due to the diffuse scattering of x rays from surface roughness that was measured in Ref. 15 in combination with the diffracted intensity of GID. Therefore, the effect of roughness on GID has become the subject of our study.

In Sec. II a theory of diffuse scattering arising from surface roughness as well as correlated and uncorrelated interface roughness in multilayers (ML's) is presented for GID. Our model is based on the dynamical theory of GID in multilayers[26–28] and the distorted-wave Born approximation.[29–32] The results are general for GID and extremely asymmetric x-ray diffraction, and are applicable in the case of normal lattice strains in multilayers.

In Sec. III we derive expressions for the diffuse scattering observed in GID with different experimental setups. In Sec. IV the theory is applied to the explanation of Ref. 15, where GID curves were taken from a sample with strong surface roughness produced by etching.

In Sec. V some numerical examples demonstrating the role of diffuse scattering in GID studies of semiconductor multilayers are given. The effect of the correlation between roughness of different interfaces is discussed. Calculations are carried out for different experimental geometries.

In Sec. VI we describe a high-resolution GID experiment carried out with an AlAs/GaAs superlattice at the optical

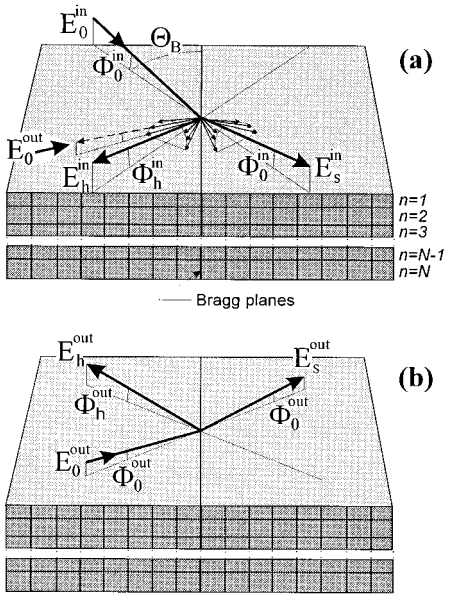

FIG. 1. Schematic layouts of grazing-incidence x-ray diffraction for (a) a real incident wave $E_0^{\rm in}$ and (b) for an ''imaginary'' incident wave $E_0^{\rm out}$ which is inverted with respect to one of diffuse scattered waves shown in (a) by a dashed line. The cones in (a) schematically illustrate DS along the diffracted and reflected waves of GID. For the explanation of other vectors, see the text.

beamline of the European Synchrotron Radiation Facility (ESRF). These direct measurements of diffuse scattering in GID are compared to calculations based on our model. We conclude with some possible uses of diffuse scattering in GID and their distinction from similar scattering in total external reflection.

II. THEORY

In GID, the diffuse scattering can be observed along the directions of both diffracted and reflected beams [see Fig. 1(a)]. We restrict our consideration to the scattering along the diffracted beam, since the majority of measurements are made in this manner.[1,5–14,20,22] The analysis of the scattering along the reflected beam of GID is analogous.

The x-ray diffuse scattering is due to the deviations $\delta\chi(\mathbf{r})$ of the polarizability of the scatterer from an ''ideal'' distribution $\chi_{\rm id}(\mathbf{r})$. The most effective way for its calculation, in the lowest-order perturbation $\delta\chi(\boldsymbol{r})$, is to apply the reciprocity theorem.[32] The amplitude of DS can be represented as

$$f=(\kappa^2/4\pi)\int \mathbf{E}^{\rm out}(\mathbf{r})\,\delta\chi(\mathbf{r})\mathbf{E}^{\rm in}(\mathbf{r})\,{\rm d}^3\mathbf{r}, \qquad (1)$$

where $\mathbf{E}^{\rm in}(\mathbf{r})$ and $\mathbf{E}^{\rm out}(\mathbf{r})$ are the wavefields in the *ideal* object (with flat interfaces) produced by the incident x-ray wave and the wave backprojected to the object from the observation point, respectively (see Fig. 1). The parameter κ is the magnitude of the wave vector of these waves in vacuum. The approximation (1) is commonly referred to as the distorted-wave Born approximation (DWBA).

In case of GID, the wave fields $E^{\rm in}(\mathbf{r})$ and $E^{\rm out}(\mathbf{r})$ can be found with the help of either kinematical[33] (see also Refs. 34 and 35) or dynamical[3] diffraction theory. The kinematical theory is applicable (i) far from the Bragg peaks from perfect crystals, (ii) for imperfect (mosaic) crystal structures, or (iii) for GID from very thin layers (1-10 monolayers). The diffracted intensities in these cases are weak and given by the DWBA. Then the scattering from interface roughness can be calculated in the kinematical theory either simultaneously with the diffraction from layers[17–19] or in the second-order DWBA. The dynamical theory is applicable at all points on GID curves corresponding to bulk reflections from perfect structures. In this case, a strong diffraction intensity at the Bragg peak and the effect of diffraction on the incident and specular waves are taken into account. That is just the case for the both experiments discussed in Secs. IV and VI, where the measurements are taken near the Bragg peaks of bulk reflections. Therefore, we use the dynamical diffraction theory in order to explain the peculiarities of diffuse scattering near the Bragg peaks of GID. For the reader's convenience, a short outline of the dynamical theory is given below.

For the sake of simplicity, we neglect the changes in x-ray polarization by diffuse scattering in GID. These changes can be simply added to the model, but they are too weak (of the order of noncoplanarity of GID, i.e., $\sim 10^{-3}$) to be of an interest for present-day experiments. Our derivations below are carried out for σ polarization. The equations are simply extended for π polarization by incorporating $\cos(2\theta_B)$ in the x-ray polarizabilities $\chi_{\rm h}$ and $\chi_{\rm \bar{h}}$.

A. Some results from the dynamical theory of GID in multilayers

In the framework of the dynamical diffraction theory, the wave fields $E^{\rm in}(\mathbf{r})$ and $E^{\rm out}(\mathbf{r})$ can be found as solutions to the system of the dynamical diffraction equations in multilayers.[26–28] Let us consider x-ray Bragg diffraction in a multilayer (see Fig. 1). It is assumed to be a stack of N perfect crystalline layers with laterally matched lattice spacing, and every layer can possess its own lattice spacing in the direction normal to the surface: $a_{\rm z}^n=a_{\rm z}+\Delta a_{\rm z}^n$, where $|\Delta a_{\rm z}^n|\ll a_{\rm z}$, and index n denotes the number of the layer in the stack counted from the surface. This model corresponds to a so-called unrelaxed multilayer containing no misfit dislocations.

At the first step, we assume flat interfaces between the layers. For Bragg diffraction from a reciprocal-lattice vector $\mathbf{h}$ approximately parallel to the surface, the polarizability can be presented as the following sum over the polarizabilities of the layers:

$$\chi_{\rm flat}(\mathbf{r})=\sum_{n=1}^{N}\chi^n(\mathbf{r})\mathcal{H}(z-z_n)\mathcal{H}(z_{n+1}-z), \qquad (2)$$

$$\chi^n(\mathbf{r})=\chi_0^n+\chi_{\rm h}^n e^{\mathbf{h}_n\cdot\mathbf{r}}+\chi_{\rm \bar{h}}^n e^{-\mathbf{h}_n\cdot\mathbf{r}}. \qquad (3)$$

Here $\mathcal{H}(z)$ is the steplike Heaviside function, and z_n are the coordinates of interfaces. Reciprocal-lattice vectors $\mathbf{h}_n$ in the nth layer differ slightly from the mean vector $\mathbf{h}$ because of the variations in the normal lattice spacing between layers: $\mathbf{h}_n=\mathbf{h}+\Delta h_{zn}\mathbf{Z}$, where $|\Delta h_{zn}|\ll h$, and $\mathbf{Z}$ is a unit vector along the internal surface normal.

In dynamical Bragg diffraction, the x-ray wave field in each layer can be expanded over the sum of the transmitted and diffracted Bloch waves with wave vectors $\mathbf{k}_{0n}$ and $\mathbf{k}_{hn}=\mathbf{k}_{0n}+\mathbf{h}_n$, and amplitudes D_{0n} and D_{hn}, respectively:[36–38]

$$E_n(\mathbf{r})=D_{0n}e^{i\mathbf{k}_{0n}\cdot\mathbf{r}}+D_{hn}e^{i\mathbf{k}_{hn}\cdot\mathbf{r}}. \tag{4}$$

The amplitudes D_{0n} and D_{hn} can be treated as constants satisfying the dynamical diffraction equations in each layer:

$$\begin{aligned}\frac{k_{0n}^2-\kappa_0^2}{k_{0n}^2}D_{0n}&=\chi_0^n D_{0n}+\chi_{\bar{h}_n}^n D_{hn},\\ \frac{k_{hn}^2-\kappa_h^2}{k_{hn}^2}D_{hn}&=\chi_{h_n}^n D_{0n}+\chi_0^n D_{hn}.\end{aligned} \tag{5}$$

Making use of the fact that the lateral components of all vectors $\mathbf{k}_{0n}$ and $\mathbf{k}_{hn}$ coincide because they remain unchanged at refraction and specular reflection, and substituting [see Fig. 1(a)]: $\kappa_{0z}=\kappa\sin\Phi_0$, $\kappa_{hz}=\kappa\sin\Phi_h$, $k_{0zn}=\kappa u_n$, and $h_{zn}=\kappa\psi_n=\kappa\psi(1-\Delta a_z^n/a)$, we can rewrite equations (5) as

$$\begin{aligned}(u_n^2-\sin^2\Phi_0-\chi_0^n)D_{0n}&=\chi_{\bar{h}_n}^n D_{hn},\\ [(u_n+\psi_n)^2-\sin^2\Phi_h-\chi_0^n]D_{hn}&=\chi_{h_n}^n D_{0n}.\end{aligned} \tag{6}$$

The condition $\boldsymbol{\kappa}_h^2=\boldsymbol{\kappa}_0^2$ presuming the elastic scattering of x rays, gives

$$\sin^2\Phi_h=(\sin\Phi_0+\psi)^2-\alpha, \tag{7}$$

where $\alpha=(2\boldsymbol{\kappa}_0\mathbf{h}+h^2)/\kappa^2$ is the standard parameter for the angular deviation of the incident wave from the Bragg condition in the dynamical theory of diffraction.

The values of u_n are determined by the dispersion equation which is the condition for the existence of a solution of Eq. (6):

$$(u_n{}^2-\sin^2\Phi_0-\chi_0^n)[(u_n+\psi_n)^2-\sin^2\Phi_h-\chi_0^n]=\chi_{\bar{h}_n}^n\chi_{h_n}^n. \tag{8}$$

Equation (8) is a fourth-order polynomial equation for u_n, and has four solutions. As shown in Ref. 39, there are always two solutions corresponding to x-ray waves damping with z [$\mathrm{Im}(u_n)>0$], and two other solutions corresponding to the waves growing with z [$\mathrm{Im}(u_n)<0$]. The latter waves are usually treated as being specularly reflected from the lower interfaces of the layers. For each of the solutions, Eq. (6) gives ($j=1,\ldots,4$):

$$D_{hnj}=\frac{u_{nj}^2-\sin^2\Phi_0-\chi_0^n}{\chi_{\bar{h}_n}^n}D_{0nj}\equiv V_{nj}D_{0nj}. \tag{9}$$

The polarizabilities $\chi_{\pm h_n}^n$ correspond to vectors $\mathbf{h}_n$ which vary from layer to layer. Therefore, it is more convenient to use the expansion over $\mathbf{h}$ (see, e.g., Ref. 40):

$$\chi_{\pm h_n}^n=\chi_{\pm h}^n\exp(\mp\Delta h_z^n z). \tag{10}$$

The substitution of Eq. (10) into Eq. (9) adds the phase factor to D_{hnj} corresponding to the expansion of the x-ray wave field over $\mathbf{h}$ instead of $\mathbf{h}_n$ in (4). Thus we can transfer this phase factor from (9) to (4), and proceed to the expansion over $\mathbf{h}$ for the whole multilayer. At that, the dispersion equations (8) remain formally unchanged because the exponents on the right side cancel each other.

The amplitudes D_{0nj} can be found with the help of the boundary conditions for the x-ray waves and their derivatives at each interface.[2–4] It is convenient to present the boundary conditions in a (4×4) matrix form,[9,26–28]

$$\begin{aligned}&\mathcal{S}_v\mathcal{E}_v=\mathcal{S}_1\mathcal{F}_1^{(U)}\mathcal{D}_1,\\ &\mathcal{S}_1\mathcal{F}_1^{(L)}\mathcal{D}_1=\mathcal{S}_2\mathcal{F}_2^{(U)}\mathcal{D}_2,\\ &\ldots\\ &\mathcal{S}_{N-1}\mathcal{F}_{N-1}^{(L)}\mathcal{D}_{N-1}=\mathcal{S}_N\mathcal{F}_N^{(U)}\mathcal{D}_N.\end{aligned} \tag{11}$$

Here $\mathcal{E}_v=(E_0,0,E_s,E_h)$ and $\mathcal{D}_n=(D_{0n1},D_{0n2},D_{0n3},D_{0n4})$ are the four-component vectors composed by unknown x-ray amplitudes [E_0, E_s, and E_h are the amplitudes of the incident, specularly reflected and diffracted waves in vacuum; see Fig. 1(a)]. Parameters $\mathcal{S}_v$, $\mathcal{S}_n$, and $\mathcal{F}_n$ denote (4×4) characteristic matrices of layers:

$$\mathcal{S}_v=\begin{pmatrix}1&0&1&0\\0&1&0&1\\\sin\Phi_0&0&-\sin\Phi_0&0\\0&\sin\Phi_h&0&-\sin\Phi_h\end{pmatrix}, \tag{12}$$

$$\mathcal{S}_{nj}=\begin{pmatrix}1\\V_{nj}\\u_{nj}\\V_{nj}(u_{nj}+\psi)\end{pmatrix}, \tag{13}$$

and $\mathcal{F}_{nij}^{(U,L)}=\delta_{ij}\exp(iu_{nj}\kappa z^{(U,L)})$, where indices (L) and (U) indicate that the exponents are evaluated at the lower (upper) boundary of layer, $(L)_n=(U)_{n+1}$.

The solution to Eq. (11) is straightforward:

$$\mathcal{E}_v=S_v^{-1}\mathcal{S}_1\mathcal{F}_{t1}\mathcal{S}_1^{-1}\mathcal{S}_2\mathcal{F}_{t2}\cdots\mathcal{S}_{N-1}^{-1}\mathcal{S}_N\mathcal{F}_N^{(U)}\mathcal{D}_N, \tag{14}$$

where $\mathcal{F}_{tnij}=\delta_{ij}\exp(-iu_{nj}\kappa t_n)$ and $t_n=z^{(L)}-z^{(U)}$. After calculating the matrix product in the right-hand side of Eq. (14), we obtain four linear equations for four amplitudes: E_s, E_h, D_{0N1}, and D_{0N2}. The other amplitudes are given by Eq.(11). For the details of the numerical procedure, the reader is referred to Refs. 26–28.

B. Amplitude of diffuse scattering from individual fluctuations in interface positions

Following the approach developed for x-ray reflection by rough surfaces,[29–32] we describe rough interfaces between layers as local fluctuations $\delta z_n(\boldsymbol{\rho})$ in the interface positions ($\boldsymbol{\rho}$ is the coordinate vector along interfaces). This approach is obviously valid at length scales much greater than the interatomic distances. Then instead of (2) the polarizability of the layers is given by

$$\chi_{\rm rough}(\mathbf{r})=\sum_{n=1}^{N}\chi^{n}(\mathbf{r})\mathcal{H}[z-z_n-\delta z_n(\boldsymbol{\rho})]\times\mathcal{H}[z_{n+1}+\delta z_{n+1}(\boldsymbol{\rho})-z], \tag{15}$$

Respectively, the fluctuations of polarizability can be written as a sum over the interfaces,

$$\delta\chi(\mathbf{r})=\chi_{\rm rough}(\mathbf{r})-\chi_{\rm flat}(\mathbf{r})=\sum_{n=1}^{N}P_n(\mathbf{r})\,\delta\chi^{n}(\mathbf{r}), \tag{16}$$

where $P(\mathbf{r})$ is the steplike function introduced by analogy with Refs. 30 and 31:

$$P_n(\mathbf{r})=\begin{cases}1, & z\in\{z_n,z_n+\delta z_n(\boldsymbol{\rho})\}, \quad \delta z_n(\boldsymbol{\rho})>0\\ -1, & z\in\{z_n+\delta z_n(\boldsymbol{\rho}),z_n\}, \quad \delta z_n(\boldsymbol{\rho})<0\\ 0 & \text{elsewhere}\end{cases} \tag{17}$$

and

$$\delta\chi^{n}(\mathbf{r})=(\chi_0^{n}-\chi_0^{n-1})+(\chi_{\rm h}^{n}-\chi_{\rm h}^{n-1})e^{i\mathbf{h}\cdot\mathbf{r}}+(\chi_{\bar{\rm h}}^{n}-\chi_{\bar{\rm h}}^{n-1})e^{-i\mathbf{h}\cdot\mathbf{r}}. \tag{18}$$

Thus the perturbation of the crystal polarizability due to roughness possesses the form

$$\delta\chi^{n}(\mathbf{r})=\sum_{n=1}^{N}P_n(\mathbf{r})(\Delta\chi_0^{n}+\Delta\chi_{\rm h}^{n}e^{i\mathbf{h}\cdot\mathbf{r}}+\Delta\chi_{\bar{\rm h}}^{n}e^{-i\mathbf{h}\cdot\mathbf{r}}). \tag{19}$$

Substituting Eq. (4) and Eq. (19) into Eq. (1) we also assume[29–32] that the wave fields do not change considerably on the scale of the roughness. Then the wave fields of one of two layers forming an interface (e.g., of the lower one) can be used at both sides of the interface, and we obtain the scattering amplitude

$$f=\sum_{n=1}^{N}f_n=\frac{\kappa^2}{4\pi}\sum_{n=1}^{N}\sum_{i=1}^{4}\sum_{j=1}^{4}\int{\rm d}^2\boldsymbol{\rho}\int_{z_n}^{z_n+\delta z_n}{\rm d}z\times e^{i(\boldsymbol{\kappa}_{0}^{\rm in}+\boldsymbol{\kappa}_{0}^{\rm out})\boldsymbol{\rho}+i\kappa(u_{ni}^{\rm in}+u_{nj}^{\rm out})z}(D_{0ni}^{\rm in}+D_{{\rm h}ni}^{\rm in}e^{i\mathbf{h}\cdot\mathbf{r}})\times(\Delta\chi_0+\Delta\chi_{\rm h}e^{i\mathbf{h}\cdot\mathbf{r}}+\Delta\chi_{\bar{\rm h}}e^{-i\mathbf{h}\cdot\mathbf{r}})(D_{0nj}^{\rm out}+D_{{\rm h}nj}^{\rm out}e^{i\mathbf{h}\cdot\mathbf{r}}). \tag{20}$$

We are interested in diffuse scattering about the direction of the grazing diffracted beam. Therefore, $\boldsymbol{\kappa}_0^{\rm out}\approx-(\boldsymbol{\kappa}_0^{\rm in}+\mathbf{h})$, and it is convenient to write

$$\boldsymbol{\kappa}_0^{\rm in}=\boldsymbol{\kappa}_{0Br}^{\rm in}+\mathbf{q}^{\rm in}, \tag{21}$$

$$\boldsymbol{\kappa}_0^{\rm out}=-\boldsymbol{\kappa}_{0Br}^{\rm in}-\mathbf{h}+\mathbf{q}^{\rm out}, \tag{22}$$

$$\mathbf{q}=\mathbf{q}^{\rm in}+\mathbf{q}^{\rm out}, \tag{23}$$

where $\boldsymbol{\kappa}_{0Br}^{\rm in}$ is the vector in the incidence direction, exactly satisfying the Bragg condition. The terms in Eq. (20) containing $\exp(\pm i\mathbf{h}\cdot\mathbf{r})$ oscillate with $\boldsymbol{\rho}$ at an atomic scale and can be neglected. Then, after carrying out the integration over z, Eq. (20) is transformed to

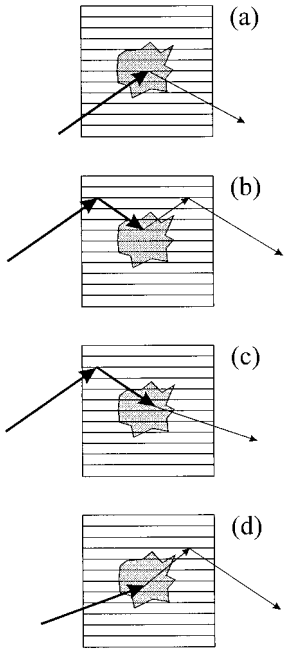

FIG. 2. Four different diagrams of x-ray scattering from a fluctuation of interface position (shaded area) in GID as given by the four terms in Eq. (25). Coherent and diffuse scattered waves are shown by thick and thin vectors, respectively. Horizontal lines present the Bragg planes in crystal.

$$f_n=\frac{\kappa^2}{4\pi}\sum_{i=1}^{4}\sum_{j=1}^{4}\mathcal{E}_{nij}\frac{\exp(iQ_{nij}z_n)}{iQ_{nij}}\times\int{\rm d}^2\boldsymbol{\rho}[e^{iQ_{nij}\delta z_n(\boldsymbol{\rho})}-1]e^{\mathbf{q}\cdot\boldsymbol{\rho}}, \tag{24}$$

where it is denoted

$$\mathcal{E}_{nij}=D_{0ni}^{\rm in}D_{0nj}^{\rm out}\Delta\chi_{\rm h}^{n}+D_{{\rm h}ni}^{\rm in}D_{{\rm h}nj}^{\rm out}\Delta\chi_{\bar{\rm h}}^{n}+(D_{{\rm h}ni}^{\rm in}D_{0nj}^{\rm out}+D_{0ni}^{\rm in}D_{{\rm h}nj}^{\rm out})\Delta\chi_0^{n}, \tag{25}$$

$$Q_{nij}=\kappa(u_{ni}^{\rm in}+u_{nj}^{\rm out}+\psi). \tag{26}$$

The four terms in Eq. (25) can be treated as shown in Fig. 2.

(i) Term 1 corresponds to the Bragg diffraction of x rays by the fluctuations of interfaces [Fig. 2(a)].

(ii) Term 2 corresponds to the triple Bragg diffraction: the incident wave is diffracted by ML, then diffracted at $-\mathbf{h}$ in the fluctuations, and diffracted by the multilayer again [Fig. 2(b)].

(iii) Term 3 corresponds to the Bragg diffraction of the incident wave by the multilayer, and the small-angle scattering of the diffracted wave by the fluctuations [Fig. 2(c)].

(iv) Term 4 corresponds to the small-angle scattering of the incident wave by the fluctuations and the Bragg diffraction of the scattered wave by the multilayer [Fig. 2(d)].

One can see that, in all four cases, x rays are scattered through the large angle $2\theta_B$ due to the diffraction from the Bragg planes. That is, the momentum transfer due to scattering from roughness is small and the intensity of DS must be much greater than that in Refs. 41 and 42. In those cases,

x-ray scattering through large angles corresponding to large momentum transfers was measured from amorphous multilayers with rough interfaces in a geometry formally similar to GID.

C. Cross section of diffuse scattering from statistical roughness

Proceeding from Eq. (24) to the cross section of diffuse scattering, we obtain

$$\frac{d\sigma}{d\Omega}=\langle|f|^2\rangle=\frac{\kappa^4}{16\pi^2}\sum_{n,n'=1}^{N}\sum_{i,i'=1}^{4}\sum_{j,j'=1}^{4}\mathcal{E}_{nij}\mathcal{E}^*_{n'i'j'}\times e^{i(Q_{nij}-Q^*_{n'i'j'})z_n}(Q_{nij}Q^*_{n'i'j'})^{-1}\times\int d^2\boldsymbol{\rho}\int \mathrm{d}^2\boldsymbol{\rho}' e^{i\mathbf{q}(\boldsymbol{\rho}-\boldsymbol{\rho}')}\times\langle e^{iQ_{nij}\delta z_n(\boldsymbol{\rho})-iQ^*_{n'i'j'}\delta z'_n(\boldsymbol{\rho})}-1\rangle, \tag{27}$$

where $\langle\ldots\rangle$ denotes averaging over random functions $\delta z_n(\boldsymbol{\rho})$ assumed to be Gaussian.

The application of the general formula[43] $\langle\exp(\Sigma_j\alpha_j x_j)\rangle=\exp(\Sigma_{jk}\alpha_j\alpha_k\langle x_j x_k\rangle/2)$, where α_j are constants and x_j are Gaussian random variables, to Eq. (27) gives

$$\frac{d\sigma}{d\Omega}=S\frac{\kappa^4}{16\pi^2}\sum_{n,n'=1}^{N}\sum_{i,i'=1}^{4}\sum_{j,j'=1}^{4}C_{nij}\mathcal{E}_{nij}C^*_{n'i'j'}\mathcal{E}^*_{n'i'j'}\times\int d^2\boldsymbol{\rho}[e^{Q_{nij}Q^*_{n'i'j'}\mathcal{K}_{nn'}(\boldsymbol{\rho})}-1]e^{\mathbf{q}\cdot\boldsymbol{\rho}}, \tag{28}$$

where $C_{nij}=\exp(iQ_{nij}z_n-\sigma_n^2Q_{nij}^2/2)/Q_{nij}$, σ_n is the rms height of roughness, $\sigma_n^2=\langle\delta z_n^2(0)\rangle$, and $\mathcal{K}_{nn'}(\boldsymbol{\rho})=\langle\delta z_n(0)\,\delta z_{n'}(\boldsymbol{\rho})\rangle$ is a correlation function. The same correlation functions proposed for diffuse scattering in x-ray TER should be valid here.[29,31,32,44,45]

Thus expression (28) for diffuse scattering in GID is formally similar to that in TER (compare Refs. 30–32 and 44–47). However, there are two essential differences. The physical difference is that diffuse scattering in TER originates from $\Delta\chi_0$ (the fluctuations of the mean target density), while in GID it is mainly due to $\Delta\chi_h$ (the crystal structure of the fluctuations). That means that diffuse scattering in GID provides information about *the degree of crystal structure perfection at interfaces*. The mathematical difference consists of the dependence of $\mathcal{E}_{nij}$ and $\mathcal{E}_{n'i'j'}$ on **q**, which is not the case in TER. Hence the DS pattern is far more complicated in GID than in TER, and depends on four diffraction angles: the angles of the incident and the scattered x-ray waves with respect to the surface and their deviations from the Bragg angle in the surface plane. An analytical integration of Eq. (28) over one of the components of **q**, like that used to reduce the calculations in the case of diffuse scattering in specular reflection, is thus not possible.

One simplification occurs when DS is studied far from the direction of propagation of the coherent diffracted beam where the Bragg diffraction of waves scattered by roughness can be neglected. Then $D^{\mathrm{out}}_{\mathrm{h}nj}=0$ and $u^{\mathrm{out}}_{nj}=\pm(\Phi_0^{\mathrm{out}2}+\chi_0^n)^{1/2}$, giving D^{out}_{0nj} as solutions to the specular reflection problem ($j=1$ and 2). This procedure can be called ''the specular-reflection approximation.'' Below, we show that it has more applications.

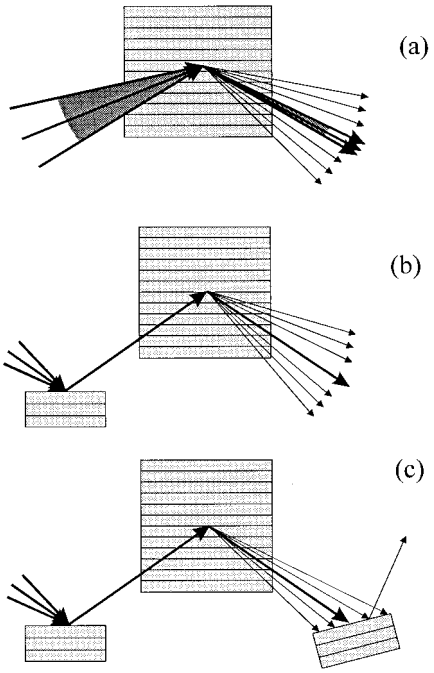

FIG. 3. Different degrees of collimation in the scattering plane of grazing-incidence x-ray diffraction: (a), (b), and (c) show single-, double-, and triple-crystal experimental schemes, respectively. Coherent and diffuse scattered waves are shown by thick and thin vectors, respectively. The incident and scattered beams are collimated and analyzed in a direction normal to the plane of the figure.

III. INTEGRATED DIFFUSE SCATTERING IN DIFFERENT TYPES OF GID EXPERIMENT

In the majority of cases the incidence and the exit angles of diffracted beam are controlled in GID experiments because these angles determine the penetration depth of GID inside the samples. However, the angles in the Bragg plane are not always controlled (see Fig. 3), and that provides some averaging of the pattern and simplification of Eq. (28).

The general formula (28) is applicable in the case of triple-crystal measurements only, when the incident beam is collimated and the scattered beam is analyzed in two planes [Fig. 3(c)]. That would be the most informative case, but the low intensity of GID might impose serious experimental limitations.

A. Single-crystal scheme: No angular resolution in the Bragg plane

Some authors[48,27,12] have performed measurements where the incident beam is collimated in Φ_0, but not in θ, and the diffracted waves are separated over their exit angles by a slit or a position-sensitive detector (PSD). This single-crystal scheme[49] is based on Eq. (7), where $\alpha=-2\sin(2\theta_B)(\theta-\theta_B)\sim10^{-5}$ is proportional to the deviation of the in-plane angle θ from the kinematic Bragg angle θ_B. The large width of Bragg peaks for Φ_0 and $\Phi_h\sim\sqrt{\alpha}\sim10^{-2}$–$10^{-3}$ makes these

measurements very convenient. However, the coherent reflection and diffuse scattered radiation are all counted together [see Fig. 3(a)].

If neither the in-plane angle of the incident or diffracted beam is collimated, then waves with large Bragg deviations dominate in the incident and scattered fans, and the solutions to the specular reflection problem can be used for both $E^{\rm in}(\mathbf{r})$ and $E^{\rm out}(\mathbf{r})$. Thus the dynamical diffraction problem of GID need not be considered for the calculations of DS at all. The experiment integrates over both the in-plane components of $\mathbf{q}$, providing $\delta(x)\delta(y)/\kappa^2$ in integral (28). Thus one finds

$$\frac{d\sigma_1}{d\Omega}=S\frac{\kappa^2}{16\pi^2}\sum_{n,n'=1}^{N}\sum_{i,i'=1}^{2}\sum_{j,j'=1}^{2}C_{nij}\Delta\chi_{\rm h}^{n}D_{0ni}^{\rm in}D_{0nj}^{\rm out}\times(C_{n'i'j'}\Delta\chi_{\rm h}^{n'}D_{0n'i'}^{\rm in}D_{0n'j'}^{\rm out})^{*}\times[e^{Q_{nij}Q_{n'i'j'}^{*}\mathcal{K}_{nn'}(0)}-1]. \tag{29}$$

As follows from Eq. (29), the DS measured in the single-crystal scheme is completely determined by $\mathcal{K}_{nn'}(0)$. In the case where the roughness of different interfaces is completely uncorrelated, $\mathcal{K}_{nn'}(0)=\sigma_n^2\delta_{nn'}$, the measurements of integral DS provide the rms roughness height.

In the case of small completely correlated roughness, where $\mathcal{K}_{nn'}(0)=\sigma_n\sigma_{n'}$ and the exponent in (29) can be expanded ($\sigma_n Q_{nij}\ll 1$), formula (29) for the diffuse scattering becomes very similar to that for the intensity of coherent GID calculated in the DWBA (see, e.g., Ref. 22):

$$\frac{d\sigma_1}{d\Omega}=\frac{S}{16\pi^2}\left|\sum_{n=1}^{N}\sum_{i,j=1}^{2}\sigma_n\kappa\Delta\chi_{\rm h}^{n}D_{0ni}^{\rm in}D_{0nj}^{\rm out}\times e^{i\kappa(u_{ni}^{\rm in}+u_{nj}^{\rm out}+\psi)z_n-\sigma_n^2\kappa^2(u_{ni}^{\rm in}+u_{nj}^{\rm out}+\psi)^2}\right|^2. \tag{30}$$

The expression for GID differs from (30) by the substitution of $\chi_{\rm h}$ instead of $\sigma_n\kappa\Delta\chi_{\rm h}^{n}$. The consequences of this analogy are discussed in Sec. V, where we give some numerical examples.

B. Double-crystal scheme: Partial angular resolution in the Bragg plane

In some more advanced (double-crystal) experiments, the incident beam is collimated in the Bragg plane, while the entire in-plane spread of the scattered beam is accepted [Fig. 3(b)]. Then the ''specular reflection'' approximation can be applied to $E^{\rm out}(\mathbf{r})$ and, additionally, one can average Eq. (28) over the components of $\mathbf{q}$ normal to $\boldsymbol{\kappa}_{\rm h}$. This procedure reduces the integral in (28) to a one-dimensional one,

$$\frac{d\sigma_2}{d\Omega}=S\frac{\kappa^3}{16\pi^2}\sum_{n,n'=1}^{N}\sum_{i,i'=1}^{4}\sum_{j,j'=1}^{2}C_{nij}\mathcal{D}_{ni}^{\rm in}D_{0nj}^{\rm out}\times(C_{n'i'j'}\mathcal{D}_{n'i'}^{\rm in}D_{0n'j'}^{\rm out})^{*}\times\int_{-\infty}^{\infty}dx[e^{Q_{nij}Q_{n'i'j'}^{*}\mathcal{K}_{nn'}(x)}-1]e^{q_{\rm x}x}, \tag{31}$$

where $q_{\rm x}=\mathbf{q}\cdot\boldsymbol{\kappa}_{\rm h}/\kappa$, and $\mathcal{D}_{ni}=D_{0ni}\Delta\chi_{\rm h}^{n}+D_{{\rm h}ni}\Delta\chi_0^{n}$ The same situation takes place when the incident beam is uncollimated in the Bragg plane, but the acceptance of the scattered beam is limited by an analyzer crystal.

IV. ANALYSIS OF A GID EXPERIMENT WITH AN ETCHED Ge SURFACE

The theory given in Secs. II and III has been applied to interpreting the results of the experiment in Ref. 15. In this study, carried out at the Cornell High-Energy Synchrotron Source (CHESS), the grazing-incidence diffraction was measured from (220) Ge planes at $\lambda=1.55$ Å. A double-crystal scheme of measurements was used. The incident beam was collimated in the incidence angle Φ_0 within 0.25 mrad, and in the diffraction angle within 0.0014 mrad. The sample was rocked through the Bragg angle θ_B at fixed Φ_0 = 4 mrad, and the entire scattered intensity was collected over the take-off angle $\Phi_{\rm h}$ and over the in-plane exit angle.

The sample surface consisted of two different parts: a high-quality polished part and an etched quadrant provided a spectrum of surface roughness. The measured GID curves for these two parts are presented in Figs. 4(a) and 4(b). The curve taken from a smooth surface coincides well with the theoretical calculations for the perfect case. A peculiarity of both the experimental and theoretical curves in the perfect case is the zero reflection coefficient to the left of the Bragg peak, where the diffracted wave becomes surface trapped [the angle $\Phi_{\rm h}$ becomes imaginary due to Eq.(7)]. Contrary to the smooth surface case, the experimental curve for a rough surface exhibits two nearly symmetrical shoulders at both sides of the Bragg peak. These shoulders are obviously due to diffuse scattering at surface roughness, because the effect of roughness on the coherent beam would appear to be a Debye-Waller attenuation of the intensity on the wings.[21]

The diffuse scattering has been calculated with the help of Eq. (31). In the case of only one interface and $\psi=0$, it is greatly simplified:

$$\frac{d\sigma_2}{d\Omega}=S\frac{\kappa^3}{16\pi^2}\left|D_0^{\rm out}\right|^2\sum_{i,j=1}^{2}\frac{e^{-\sigma^2(Q_i^2+Q_j^{*2})/2}}{Q_iQ_j^{*}}\mathcal{D}_i^{\rm in}\mathcal{D}_j^{\rm in*}\times\int_{-\infty}^{\infty}dx[e^{Q_iQ_j^{*}\mathcal{K}(x)}-1]e^{q_{\rm x}x}, \tag{32}$$

where $D_0^{\rm out}=2\sin\Phi_0^{\rm out}/(\sin\Phi_0^{\rm out}+u^{\rm out})$, $Q_i=\kappa(u_i^{\rm in}+u^{\rm out})$, $u^{\rm out}=(\sin^2\Phi_0^{\rm out}+\chi_0)^{1/2}$, and $u_i^{\rm in}$ are the two solutions to the dispersion equation (8) with $\mathrm{Im}(u_i^{\rm in})>0$.

Equation (32) was integrated over $\Phi_{\rm h}$, and renormalized to the reflectivity [see Eq. (2.13) in Ref. 29]:

$$|R|_{\rm DS}^2=\frac{1}{S\sin\Phi_0}\int_0^{\infty}\frac{d\sigma_2}{d\Omega}d\Phi_h. \tag{33}$$

The correlation function was chosen in the Gaussian form: $\mathcal{K}(\boldsymbol{\rho})=\sigma^2\exp(-\rho^2/\xi^2)$, where σ is the rms height and ξ is the lateral correlation length of roughness. The integration in (33) was carried out numerically.

The normalized calculated flux of DS for different ξ is presented in Fig. 4(c). The shape of DS curves strongly depends on the lateral correlation length of roughness: at greater correlation lengths DS is concentrated closer to the coherent diffracted beam of GID. The dependence of calcu-

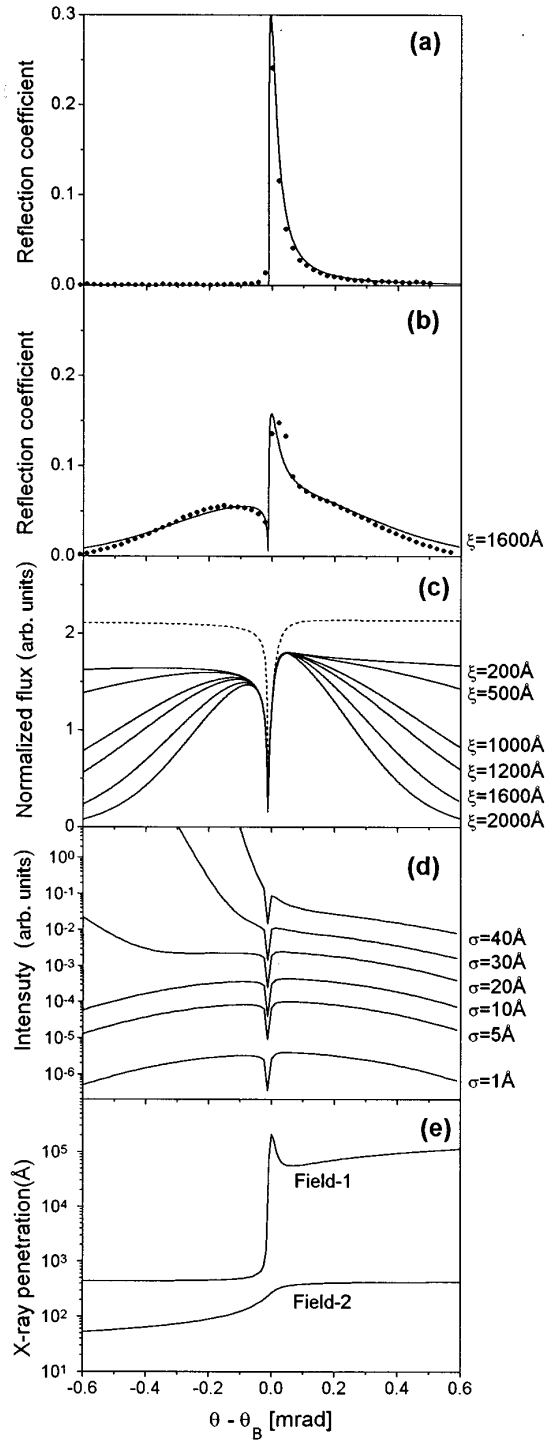

FIG. 4. Fitting of GID data measured in Ref. 15 [Ge, (220) Bragg planes, $\lambda = 1.55$ Å, and $\Phi_0 = 4$ mrad]. Data are represented by dots, and fits by solid lines. (a) Smooth surface (fit assumes GID with no diffuse scattering). (b) Rough surface (fit is GID plus DS calculated with $\xi = 1600$ Å and $\sigma = 43$ Å). (c) Calculated shape of DS curves vs correlation length of roughness (the dashed line indicates the total x-ray intensity at crystal surface). (d) Intensity of DS vs height of roughness (the DWBA diverges at $\theta - \theta_B < 0$ for $\sigma = 20$, 30, and 40 Å). (e) Penetration depth inside the crystal calculated for two wave fields $\mathcal{D}^{\rm in}_{1,2}$ of GID at $\Phi_0 = 4$ mrad [the decrease in penetration depth at $\theta - \theta_B < 0$ causes the divergence of the DWBA in (d)].

lated DS on σ is presented on Fig. 4(d). The intensity of DS quickly grows with σ, while the shape of the curves is practically independent of σ in a wide range up to $\sigma \lesssim 10$ Å. At $\sigma > 10$ Å, the DWBA starts to diverge at $\theta - \theta_B < 0$, where the diffracted wave of GID is surface trapped. This divergence is due to a small penetration depth of surface-trapped x-rays [see Fig. 4(e)]. The DWBA breaks down when the x-ray wave fields undergo large changes on the scale of the height of the roughness.

The roughness height for the case in Fig. 4(b) measured with a 3-μm profilometer tip was $\sigma \simeq 200$ Å. This value was obviously beyond the applicability of the DWBA. In particular, the DWBA fails to explain the attenuation of maximum reflectivity at the Bragg peak in Fig. 4(b). However, taking into account the weak dependence of the shape of DS curves on σ, we can fit the shape of the curves at small σ, and then extrapolate the data to higher σ where the DWBA diverges.

The fitting procedure was carried out in two steps: first, the shape of the DS curve was fitted at $\theta - \theta_B < 0$ where the coherent reflection is zero [see Fig. 4(a)]. Then the calculated DS was added to the calculated coherent reflectivity attenuated by some empirical factor $c_{\rm h}$ in order to fit the maximum of the reflection coefficient: $|R|^2_{\rm total} = c_{\rm h}|R|^2_{\rm coherent} + |R|^2_{\rm DS}$. The factor c_h was introduced to account for the relative contributions of coherent diffracted and scattered radiation when the roughness was great.

The parameters of the fit presented in Fig. 4(b) are $\xi = 1600$ Å and $c_{\rm h} = 0.4$. The roughness rms height fitted at $\theta - \theta_B > 0$, where the DWBA does not diverge is $\sigma = 43$ Å. This value is consistent with the profilometer data, since the rms roughness at $\xi = 1600$ Å need not be as great as the rms roughness at $\xi = 30\,000$ Å corresponding to the horizontal resolution limit of the profilometer. The long-wavelength roughness measured with the profilometer could not cause the DS on the tails of the curve Fig. 4(b) because the DS corresponding to the long-wavelength roughness is strongly concentrated near the Bragg peak. This roughness was probably responsible for the broadening of the experimental Bragg peak in Fig. 4(b). If, on the other hand, we consider the possibility that etching causes the crystal structure disordering, then, the parameter $\Delta\chi_{\rm h}$ in Eq. (32) would be reduced by a static Debye-Waller factor, and the same intensity of DS would be achieved with a greater σ.

Both the experiment and theory show a dip in the DS pattern at the Bragg peak. In Ref. 15 this dip was supposed to be due to a cutoff of the maximum roughness wavelength ξ to which the experiment should be sensitive because of the limited coherence length of the diffracted beam ($\simeq 3$ μm). The theory presented here contains no assumptions on the coherence length of the source, and the interpretation of this effect is different. As follows from Eqs. (31) and (32), the intensity of DS in the double-crystal scheme is approximately proportional to the total intensity of the x-ray wave field illuminating the interface:

$$\frac{d\sigma_2}{d\Omega} \sim \sum_{i,i'=1}^{2} \mathcal{D}^{\rm in}_i \mathcal{D}^{\rm in}_{i'}{}^{*} \approx \left| \Delta\chi_0 \sum_{i=1}^{2} (D^{\rm in}_{0i} + D^{\rm in}_{\rm hi}) \right|^2 = |\Delta\chi_0 (E^{\rm in}_0 + E^{\rm in}_{\rm s} + E^{\rm in}_{\rm h})|^2. \tag{34}$$

The right side of Eq. (34) exhibits a dip at $\theta \approx \theta_{220}$, providing the minimum in DS [see the dashed line in Fig. 4(c)]. Thus, the observed effect has the same origin as the Yoneda peaks[50,29] in x-ray DS and the secondary emission yield appearing near the critical angle for TER. Yoneda peaks are due to the enhancement of x-ray intensity at the surface near the critical angle for total *external* reflection. Here we have a dip in intensity at the atomic planes near the Bragg angle, which is matched in this instance with the threshold angle for total *internal* reflection [with the angle θ, where Φ_h becomes an imaginary quantity due to Eq. (7) and the diffracted wave becomes surface trapped]. This dip provides a minimum in DS in Fig. 4(b) as well as a minimum in the fluorescence yield from lattice sited atoms which was observed in GID standing wave experiment.[51,52] Therefore, our case can be referred to as an ''anti-Yoneda effect.''

At $\psi \neq 0$, the critical angle for total internal reflection given by Eq. (7) may not coincide with the Bragg angle. Then two dips in DS are predicted by our theory, the dip at the critical angle for total internal reflection being stronger than that at the Bragg angle.

V. DIFFUSE SCATTERING IN MULTILAYERS

In the case of multiple and periodic rough interfaces, the effects of roughness become much more prominent. We have carried out calculations for a sample similar to that discussed in Refs. 27 and 31: an AlAs/GaAs superlattice consisting of 20 periods of 125 Å AlAs and 95 Å GaAs on a [001]-oriented GaAs substrate. The calculations assumed a (220) Bragg reflection of $\sigma-$polarized incident x rays with $\lambda = 1.5$ Å and $\Phi_0 = 0.3°$. The correlation function was chosen in the form suggested by Ming *et al.*,[44]

$$\mathcal{K}_{nn'}(\boldsymbol{\rho}) = \sigma_n \sigma_{n'} e^{-(\rho/\xi)^2} e^{-|z_n - z_{n'}|/\xi_z}, \tag{35}$$

with a rms roughness height $\sigma_n = 5$ Å and a lateral correlation length $\xi = 2000$ Å.

The calculated intensity of DS for the single-crystal case of GID renormalized to a reflectivity as in Eq. (33) is presented in Fig. 5 as a function of exit angle Φ_h. Curves 1 and 2 correspond to the uncorrelated ($\xi_z = 0$) and completely correlated ($\xi_z = \infty$) roughness of interfaces, respectively. One can see that in both the cases the curves exhibit multilayer Bragg peaks at the same angular positions as the peaks of coherent GID (curves 3 and 4). Therefore, it is difficult to separate the diffracted and diffuse intensities. In the case of correlated roughness, the DS about the multilayer Bragg peaks becomes much more prominent, and the intensity at large Φ_h is comparable to the intensity of coherent GID. The shape of the DS curve is very similar to that of coherent GID, as given by (30) and well seen in Fig. 5, but the decrease in DS intensity with Φ_h is slower. These results may explain the discrepancies between the theory and experiment at high angles observed in the single-crystal measurements of GID in multilayers in Ref. 27.

To distinguish the effect of DS on single-crystal GID curves, one might measure the parameters of roughness by x-ray reflectivity and diffuse scattering in TER, substitute the roughness value into Eq. (29), and subtract the calculated DS from the measured GID curves. However, as follows from Eq. (29) and Fig. 2, the DS contributing to the single-crystal

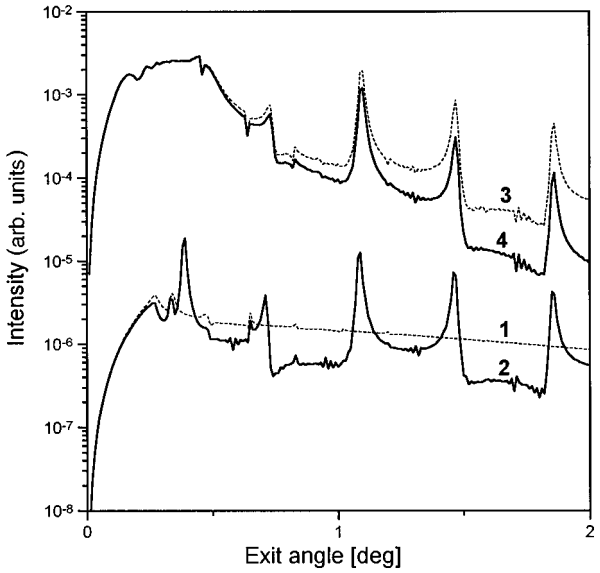

FIG. 5. Calculated x-ray reflectivity curves vs the takeoff angle for the single-crystal scheme of GID. The curves are for a 20-period AlAs/GaAs superlattice ($t_{AlAs} = 125$ Å and $t_{GaAs} = 95$ Å) on a [001] GaAs substrate. The parameters of the calculations are as follows: (220) reflection, $\lambda = 1.5$ Å; $\Phi_0 = 0.3°$, $\sigma = 5$ Å, and $\xi = 2000$ Å. Curves 1 and 2 show DS for uncorrelated ($\xi_z = 0$) and completely correlated ($\xi_z = \infty$) roughnesses of interfaces, respectively. Curves 3 and 4 present the coherent GID reflection for flat and rough interfaces, respectively.

GID measurements is due to fluctuations in the crystal structure $\Delta\chi_h$, while the parameters of roughness given by x-ray reflectivity refer to the fluctuations of material density $\Delta\chi_0$. In the case where the crystal structure is destroyed by roughness, the data of TER and GID may disagree: the latter may exhibit a reduced intensity corresponding to a smaller σ. Then, to isolate the diffuse component of GID, one has to select scattered radiation in double- or triple-crystal measurements.

A comparison between the diffuse scattering in TER and GID can be used for investigating the crystal structure of rough interfaces. In our model, one can add a Debye-Waller factor for $\Delta\chi_h$ and $\Delta\chi_{\bar{h}}$ in Eq. (25) describing the attenuation of polarizabilities due to disordering of the crystal structure at rough interfaces. The value of this Debye-Waller factor can be found from the difference in σ given by TER and GID. Thus the diffuse scattering in GID can deliver a measure of crystal structure ordering at rough interfaces. This information is not accessible by conventional x-ray scattering techniques.

The calculations for the double-crystal scheme of GID are presented in Fig. 6 for noncorrelated (a) and completely correlated (b) interface roughness in multilayers. Due to the in-plane angular collimation of the incident x rays, for each $\theta - \theta_B$ the diffracted wave exits the crystal at the certain angle Φ_h, as given by Eq.(7). The exit angle of the diffracted wave at different $\theta - \theta_B$ is traced on the maps by thick solid stripes. The intensity at all other points on the maps can be attributed to DS. Thus a separation of coherent and diffuse scattering is possible.

The maps in Fig. 6 clearly show the bunching of the DS into resonance diffraction sheets (RDS's) for correlated in-

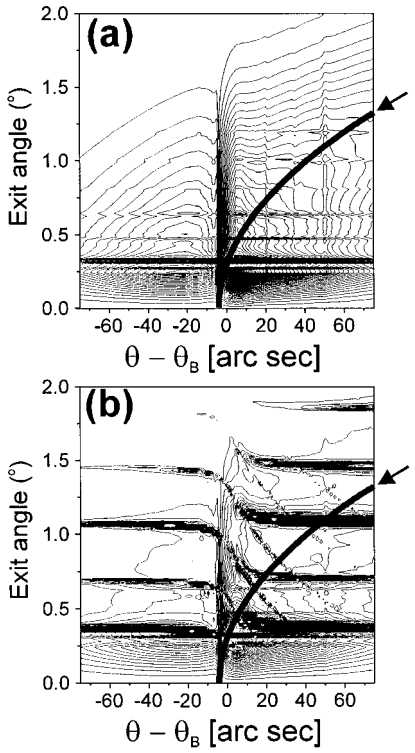

FIG. 6. Calculated maps of diffuse scattering for the double-crystal scheme of GID experiments. The parameters of the calculations are the same as in Fig. 5. The equal-intensity map (a) is for uncorrelated interface roughness, and (b) is the same for completely correlated roughness. Thick stripes marked by arrows show the position of the coherent wave of GID.

terface roughness. This effect is completely analogous to the formation of RDS's (''Holy bananas'') in DS during x-ray specular reflection.[31] The vertical black fringe at $\theta \simeq 0$ corresponds to the anti-Yoneda minimum in DS which we have discussed above for scattering from a rough surface.

Another interesting peculiarity displayed by Fig. 6(b) is the appearance of RDS's at negative $\theta - \theta_B$ where the diffracted wave of GID is surface trapped and cannot exit the crystal. This effect is surprising because the surface-trapped wave has a small penetration depth inside the crystal [see Fig. 4(e)], and one could expect only a few interfaces contributing to DS at these angles. However, two types of x-ray wave fields are generally excited in the crystal under GID: one wave can be roughly connected to the diffracted wave in vacuum, and the other one to the incident wave. The angle of the latter wave to the surface is not small in our example, thus providing a greater penetration depth. This effect can be used for the experimental measurements of DS because the separation of the diffracted beam is unnecessary. We note a small difference in the positions of RDS's at positive and negative $\theta - \theta_B$.

As long as the coherent and diffuse scattering can be discriminated with the double-crystal scheme of the GID experiment, the triple-crystal scheme [Fig. 3(c)] is not of particular interest. The situation might change in the case of relaxed superlattices containing a distribution of lattice spacings along the lateral direction. In this case, Eq. (7) becomes inapplicable,[53] and a fan of diffracted waves with different Φ_h can exit the crystal at each $\theta - \theta_B$. Diffuse and coherent scattering could be separated out in this case by means of the triple-crystal scheme. The calculations of DS for relaxed superlattices could be performed using Eq. (1) and the wave fields of GID found in Ref. 53.

VI. MEASUREMENTS OF DIFFUSE SCATTERING FROM AlAs/GaAs MULTILAYER

In order to provide a comprehensive test of our theory, we have undertaken high-resolution measurements of GID from a 20-period AlAs/GaAs superlattice (SL). The GID experiment has been carried out at the optics beamline BL10 of ESRF.

The superlattice grown by molecular-beam epitaxy on a [001] GaAs substrate was characterized in the laboratory by x-ray Bragg diffraction, x-ray specular reflection, and nonspecular x-ray scattering. A θ-2θ scan near the (004) Bragg peak did not reveal any strain relaxation, indicating that the superlattice possessed a laterally matched crystal structure. The thickness of the layers obtained from the fitting of this scan was $t_{\mathrm{AlAs}} = (154 \pm 1)$ Å, and $t_{\mathrm{GaAs}} = (73 \pm 1)$ Å. The x-ray-diffraction data also indicated a sample surface miscut of $(-0.38 \pm 0.02)°$ along [110]. The x-ray specular reflection θ-2θ scans confirmed the thickness of AlAs and GaAs layers and revealed a surface transition layer with a thickness of (18 ± 2) Å, probably due to natural oxidation. A fit to the specular reflection curve gave the rms height of interface roughness $\sigma_i = (4 \pm 0.5)$ Å. Finally, the longitudinal and transverse scans of nonspecular x-ray scattering at grazing incidence (θ-2θ scans with θ offsets of the sample and θ scans at fixed 2θ positions of the detector, respectively) were carried out in order to determine the vertical and lateral correlation lengths of roughness. The longitudinal scans exhibited very sharp RDS maxima corresponding to a complete correlation between the roughness of different interfaces. Therefore, the data were fitted with the simple correlation function (35) assuming $\xi_z = \infty$. The transverse scan along RDS-8 ($2\theta = 3.172°$) and the corresponding fit are shown in Fig. 7. The fit consists of two independent contributions of interface and surface roughness, which explain the central part of the curve and the Yoneda peaks at the wings, respectively. The fitted parameters are $\sigma = 4$ Å, $\xi = 3000$ Å for the interface roughness, and $\sigma = 9$ Å, $\xi = 500$ Å for the surface roughness. The height of the surface roughness corresponds to half of the thickness of the surface transition layer found by reflectometry. The lower-order RDS indicated a more complicated spectrum of roughness. For example, the transverse scan at RDS-5 ($2\theta = 2.033°$) was better explained by a combination of the same surface roughness and a sum of interface roughness with $\sigma = 4$ Å, $\xi = 4500$ Å, $\sigma = 3$ Å, $\xi = 3000$ Å and $\sigma = 2$ Å, $\xi = 1500$ Å. However, in the first approximation the parameters $\sigma = 4$ Å, $\xi = 3000$ Å found at RDS-8 were applied to modeling the results of the GID experiment.

The experimental configuration of the GID experiment is shown in Fig. 8. The grazing-incidence diffraction was measured from the (220) AlAs/GaAs planes in the double-crystal scheme corresponding to Fig. 3(b), and similar to the experiment at CHESS.[15] However, in contrast to Ref. 15, the angular spectrum of the diffracted beam was analyzed with a

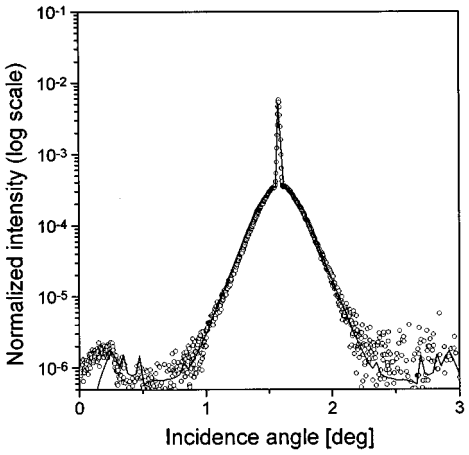

FIG. 7. Transverse scan through the eighth-order resonance sheet ($2\theta = 3.172°$) of x-ray diffuse scattering taken from an AlAs/GaAs superlattice far from diffraction conditions. Experimental data are represented by circles, and the theoretical fit by the solid line. The fit is the sum of contributions of completely correlated interface roughness ($\sigma = 4$ Å, $\xi = 3000$ Å) and surface roughness ($\sigma = 9$Å, $\xi = 500$ Å).

linear PSD, and the experimental setup was optimized in order to provide a good separation of GID and DS.

A Si(111) double-crystal monochromator was tuned to $\lambda = 1.40$ Å. The crystals in the monochromator were slightly offset in angle to suppress the third and higher harmonics.[54] The divergence of the x-ray beam in the vertical plane over Φ_0 was mainly determined by the monochromator since the vertical divergence of synchrotron radiation at ESRF is $\simeq 1$ sec of arc. The collimation of the beam in the horizontal plane over θ was provided by five (220) reflections in a channel-cut Si crystal. The five-reflection collimator was used to suppress the tails of the x-ray beam and provide a better discrimination of GID and DS at the position-sensitive detector.

The estimated parameters of the incident beam at the sample were: $\Delta\lambda/\lambda \lesssim 1.2\times 10^{-4}$, $\Delta\Phi_0 \lesssim 6$ sec of arc, and $\Delta\theta \lesssim 4$ sec of arc. The last parameter is given with account of the dispersion effect caused by the difference in the Bragg angles of Si and GaAs (220) reflections. The horizontal divergence was examined by recording a (220) rocking curve

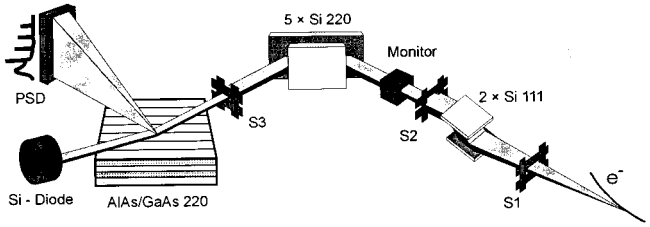

FIG. 8. The scheme of the high-resolution GID experiment carried out on the optical beamline of ESRF. The linear position-sensitive detector (PSD) provided an angular analysis of radiation scattered along the diffracted beam of GID. The intensity of the specular x-ray beam was recorded integrally using a Si photodiode. For the integral GID measurements presented in Fig. 9, the PSD was replaced by a scintillation counter.

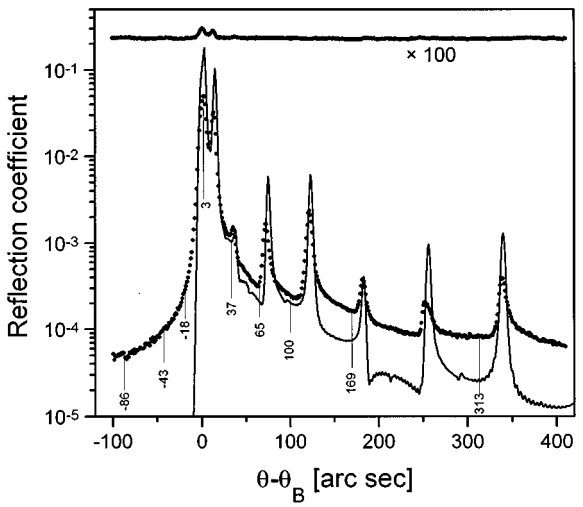

FIG. 9. Double-crystal rocking curve of GID taken from the AlAs/GaAs superlattice at $\Phi_0 = 0.5°$. Dots represent experimental data, and the solid line is a theoretical simulation convoluted with the rocking curve of the five-reflection monochromator. The top line is the magnified reflection coefficient for the specular x-ray beam. Vertical marks indicate the sample positions where PSD spectra of diffracted intensity were taken (see Fig. 11).

from a Ge wafer: the width of the Bragg peak corresponded to the calculated value. The angular resolution of the PSD over the takeoff angle was 15 sec of arc.

The front of the beam impinging on the sample was restricted by the output slits $S3$ with vertical and horizontal sizes of 0.04 and 0.2 mm, respectively. This provided an illuminated area smaller than the sample size, and eliminated edge reflections. The primary and the secondary slits $S1$ and $S2$ restricted the beam front to 1×2 mm^2 and 0.1×1 mm^2, respectively, and reduced the background in the experimental hutch.

In the first step of the experiment, the PSD was replaced by a scintillation counter. The diffracted beam was recorded while scanning θ as in Ref. 15 with no separation of the coherent and diffuse components. A second counter (Si photodiode) simultaneously recorded the rocking curves of the specularly reflected x-ray beam. Figure 9 presents the measured and calculated rocking curves for the incidence angle $\Phi_0 = 0.5°$. The parameters for the calculations are taken from the laboratory data presented at the beginning of this section and the algorithm is described in Sec. II and elsewhere.[21] The experiment clearly demonstrates the high quality of the superlattice: (i) the half-widths of the Bragg peak and the superlattice peaks correspond to the calculated parameters; and (ii) the rocking curve of the specular beam exhibits a maximum at the first superlattice Bragg peak, thus proving that the diffraction is dynamical.

At the same time, the reflectivity at the wings of measured GID curve is noticeably higher than expected and is probably due to DS. Figure 10 shows the map of DS calculated for the experimental conditions according to (31). In contrast to the example given in Fig. 6(b), the DS is concentrated along the diffracted beam of GID because of a greater lateral correlation length. However, a characteristic pattern of DS with periodic superlattice peaks in two directions is well developed. The SL peaks parallel to the θ-axis are especially

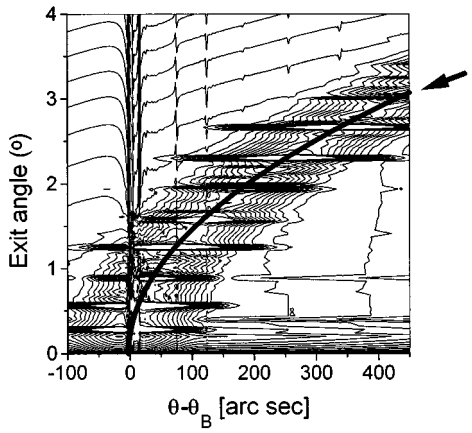

FIG. 10. Calculated map of diffuse scattering in GID ($\Phi_0 = 0.5°$) for the AlAs/GaAs superlattice studied at ESRF. The thick stripe marked by the arrow shows the position of the coherent wave of GID. The theoretical curves in Fig. 11 are the sections of this map drawn along the vertical axis at different $\theta - \theta_B$.

strong, and should be clearly seen in PSD observations which cut the map along the Φ_h axis.

The PSD spectra have been taken at different θ-positions of the sample as marked in Fig. 9. The results are shown in Fig. 11. The curves in the figure are vertically shifted with respect to each other as explained in the figure caption. The experiment is compared to the theoretical curves, which consist of four parts

$$I_{\mathrm{Total}}(\Phi_h, \Delta\theta) = I_{\mathrm{GID}}(\Phi_h, \Delta\theta) + I_{\mathrm{DS}}^{\mathrm{IF}}(\Phi_h, \Delta\theta) + I_{\mathrm{DS}}^{\mathrm{Surf}}(\Phi_h, \Delta\theta) + I_{\mathrm{Backgr}}. \quad (36)$$

Here $I_{\mathrm{GID}}(\Phi_h, \Delta\theta) = R_{\mathrm{GID}}[\alpha(\Phi_h)] R_5[\alpha(\Phi_h) - \Delta\alpha(\Delta\theta)]$ is the product of x-ray Bragg reflections from the sample and the five-reflection collimator, respectively; $\alpha(\Phi_h)$ is the x-ray Bragg deviation for the sample given by Eq. (7), and $\Delta\alpha(\Delta\theta) = -2\sin(2\theta_B)\Delta\theta$ is the difference in α for collimator and sample due their angular misalignment $\Delta\theta$ corresponding to a given PSD spectrum. The terms $I_{\mathrm{DS}}^{\mathrm{IF}}$ and $I_{\mathrm{DS}}^{\mathrm{Surf}}$ are the DS intensities for the interface and surface roughness, respectively, calculated according to Eq. (31) with the parameters found from the laboratory measurements. Finally, I_{Backgr} is a constant term equal to the experimental background.

Different terms in Eq. (36) explain different peculiarities of the experimental spectra in Fig. 11. The coherent reflection provides the floating peaks marked by arrows. The position of these peaks is given by Eq. (7) with $\alpha = \Delta\alpha(\Delta\theta)$. The strongest effect of coherent reflection is observed at $\Delta\theta = 3$ arc sec, where two coherent peaks are found. At $\Delta\theta < 0$, the contribution of coherent reflection is small and invisible on the spectra.

DS due to interface roughness forms regular superlattice peaks, with a maximum intensity around the position of the coherent reflection, as expected from the map presented in Fig. 10. At $\Delta\theta < 0$ and $\Delta\theta \geq 65$ arc sec, the integrated intensity of DS peaks exceeds the integrated intensity of the diffraction peak itself, thus explaining the high-intensity wings of the experimental curve in Fig. 9. It is worth noting that su-

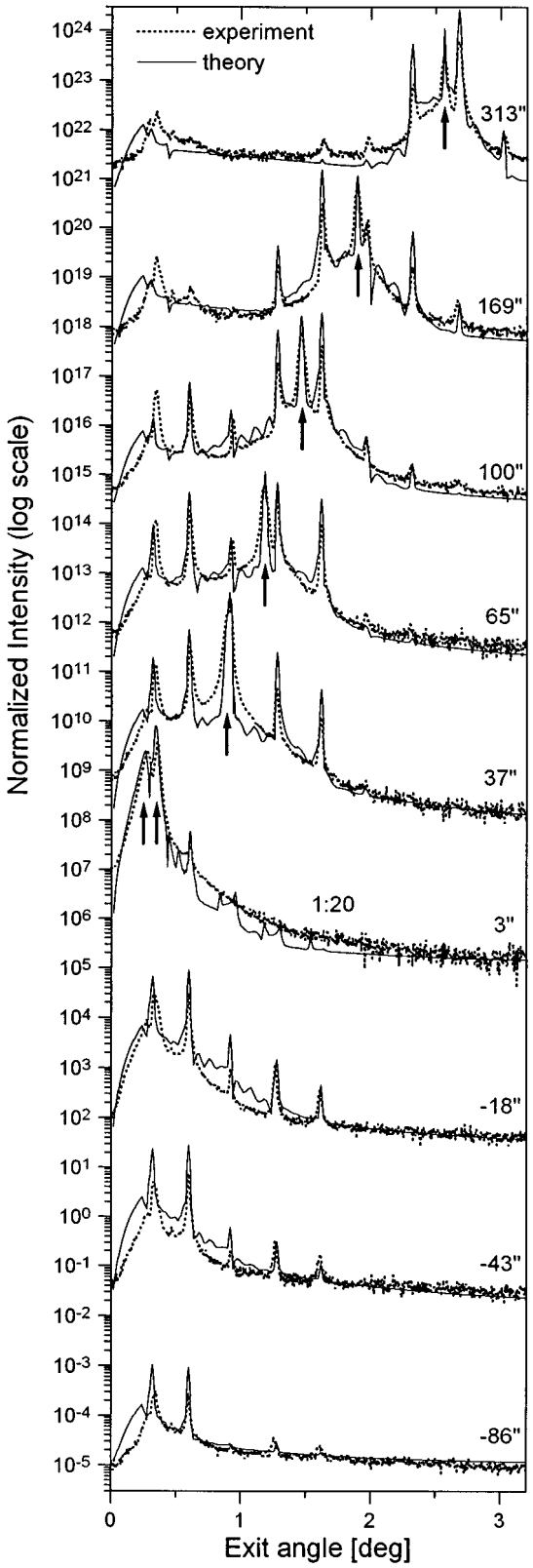

FIG. 11. PSD spectra of GID intensity vs exit angle at $\Phi_0 = 0.5°$ and different $\theta - \theta_B$ for the AlAs/GaAs superlattice. Dots present experimental data, and solid lines are calculations with parameters taken from the laboratory studies of the sample. Arrows mark coherent peaks. The curves are successively shifted by 10^3 for clarity. The central curve is then reduced by a factor of 20 because of its high intensity.

perlattice peaks are observed for $\Delta\theta<0$. This proves that the x-ray wave field in GID possesses greater penetration inside the superlattice, even though the diffracted wave is surface trapped.

Finally, the surface roughness provides a maximum in DS near the critical angle of TER (at $\Phi_h\sim 0.3°$) for the data corresponding to $\Delta\theta=169$ and 313 arc sec, and $\Delta\theta<0$. Here we have found that the intensity of DS calculated due to the surface roughness with $\sigma=9$ Å was a factor of 4 greater than observed in the experiment. The theoretical curves presented in Fig. 11 correspond to $\sigma=4.5$ Å, half of the value determined from the laboratory measurements. We suggest that the difference in the observed σ values is due to the distinction between diffuse scattering in TER and GID: the diffuse scattering in TER is proportional to $\Delta\chi_0^2$, while that in GID is mainly given by $\Delta\chi_h^2$, a measure of the atomic ordering in roughness. The crystal structure at the surface could be partially destroyed by the oxidation, giving rise to weaker DS in GID. Thus our experiment confirms the conclusion derived in Sec. V that the measurements of DS in GID may provide information on atomic ordering at interfaces which is not accessible by DS in TER.

While the agreement between our theory and experiment is reasonable, some discrepancies can be attributed to the simplified model of the correlation function used in the calculations. It is worth noting that no diffuse scattering due to crystal structure defects in the superlattice was observed. As shown in Refs. 55 and 56, a peak of DS due to pointlike defects could be expected at $\Phi_h|_{\alpha=0}\approx 0.24°$. Some discrepancies between the theory and experiment at small Φ_h near the critical angle of TER might be due to this kind of scattering, but the scattering from interface roughness was the major contribution.

VII. CONCLUSIONS

We have presented a theory and experimental results on the effects of roughness in grazing-incidence diffraction by crystals. It has been shown that surface and interface roughness in crystals can give rise to x-ray diffuse scattering about the diffraction beams of GID. The theoretical model is based on the distorted-wave Born approximation[29] and the dynamical theory of GID by multilayers.[26–28] The model can be applied to asymmetric x-ray diffraction and to the diffraction of neutrons. Expressions have been obtained for GID experiments in different geometries. The effect of interface-interface roughness correlations on x-ray diffuse scattering in GID has been taken into account. It has been demonstrated that in the case of periodic interfaces, interface-interface correlations give rise to the formation of resonance sheets in DS similar to ''Holy bananas''[31] in small-angle x-ray scattering.

When applied to the analysis of GID data taken from a Ge crystal etched to provide a roughened surface, the theory obtains the observed diffracted intensity and diffuse scattering. The intensity shoulder on the experimental curve at $\theta-\theta_B<0$, where the GID intensity must otherwise be zero, has been explained by diffuse scattering from the surface roughness. A dip in the diffuse scattering near the Bragg peak can be attributed to an ''anti-Yoneda'' effect.

High-resolution measurements of GID have been reported. This approach allowed the diffracted flux from an AlAs/GaAs superlattice to be resolved into GID and diffuse scattering due to correlated interface roughness. The experimental results are in good agreement with the theory. Measurements of diffuse scattering in GID are sensitive to atomic ordering in roughness, thereby providing information which is not accessible by conventional small-angle x-ray scattering.

ACKNOWLEDGMENTS

One of us (S.A.S.) is pleased to thank S. Sinha (Argonne National Laboratory) and V. Kaganer (Institute of Crystallography, Moscow) for stimulating discussions. We also wish to acknowledge the valuable advice from T. Baumbach (Institut Laue-Langevin, Grenoble) and J. Härtwing and U. Lienert (ESRF) concerning the experimental scheme, and we are especially grateful to R. Hey (Paul-Drude Institute, Berlin) for the preparation of the AlAs/GaAs superlattice.

*Permanent address: Institute for Nuclear Problems, 11 Bobruiskaya St., Minsk 220050, Republic of Belarus.

[1] W. C. Marra, P. Eisenberger, and A. Y. Cho, J. Appl. Phys. **50**, 6927 (1979).
[2] V. G. Baryshevskii, Pis'ma Zh. Tekh. Fiz. **2**, 112 (1976) [Sov. Tech. Phys. Lett. **2**, 43 (1976)].
[3] A. M. Afanas'ev and M. K. Melkonyan, Acta Crystallogr. A **39**, 207 (1983).
[4] T. Jach, P. L. Cowan, Q. Shen, and M. J. Bedzyk, Phys. Rev. B **39**, 5739 (1989).
[5] A. L. Golovin and R. M. Imamov, Phys. Status Solidi A **80**, K63 (1983).
[6] P. A. Aleksandrov *et al.*, J. Appl. Crystallogr. **18**, 27 (1985).
[7] A. L. Golovin, R. M. Imamov, and E. A. Kondrashkina, Phys. Status Solidi A **88**, 505 (1985).
[8] R. M. Imamov *et al.*, Poverkhn. Fiz. Khim. Mekh. (USSR) **3**, 41 (1987).
[9] S. Rugel, G. Wallner, H. Metzger, and J. Peisl, J. Appl. Crystallogr. **26**, 34 (1993).
[10] A. A. Williams *et al.*, Phys. Rev. B **43**, 5001 (1991).
[11] V. H. Etgens *et al.*, Phys. Rev. B **47**, 10 607 (1993).
[12] U. Pietsch *et al.*, J. Appl. Phys. **74**, 2381 (1993).
[13] S. Grotehans *et al.*, Phys. Rev. B **39**, 8540 (1989).
[14] D. Bahr, W. Press, R. Jebasinski, and S. Mantl, Phys. Rev. B **51**, 12 223 (1995).
[15] T. Jach, D. B. Novotny, M. J. Bedzyk, and Q. Shen, Phys. Rev. B **40**, 5557 (1989).
[16] V. Holý, T. Baumbach, and M. Bessiere, J. Phys. D **28**, A220 (1995).
[17] H. A. van der Vegt *et al.*, Phys. Rev. B **51**, 14 806 (1995).
[18] H. A. van der Vegt, W. J. Huisman, P. B. Howes, and E. Vlieg, Surf. Sci. **330**, 101 (1995).
[19] M. Sauvage-Simkin *et al.*, Phys. Rev. Lett. **75**, 3485 (1995).
[20] R. M. Imamov, E. A. Kondrashkina, D. V. Novikov, and S. A. Stepanov, Kristallografiya **32**, 852 (1987) [Sov. Phys. Crystallogr. **32**, 501 (1987)].
[21] S. A. Stepanov and R. Köhler, J. Appl. Phys. **76**, 7809 (1994).
[22] G. T. Baumbach, S. Tixier, U. Pietsch, and V. Holý, Phys. Rev. B **51**, 16 848 (1995).
[23] P. A. Aleksandrov, A. M. Afanas'ev, and M. K. Melkonyan, Kri-

stallografiya **26**, 1275 (1981) [Sov. Phys. Crystallogr. **26**, 725 (1981)].
[24] L. Névot and P. Croce, Rev. Phys. Appl. **15**, 761 (1980).
[25] A. Caticha, Phys. Rev. B **52**, 9214 (1995).
[26] S. A. Stepanov, Kristallografiya **39**, 221 (1994) [Sov. Phys. Crystallogr. **39**, 182 (1994)].
[27] S. A. Stepanov, U. Pietsch, and G. T. Baumbach, Z. Phys. B **96**, 341 (1995).
[28] S. A. Stepanov and R. Köhler, J. Phys. D **27**, 1923 (1994).
[29] S. K. Sinha, E. B. Sirota, S. Garoff, and H. B. Stanley, Phys. Rev. B **38**, 2297 (1988).
[30] V. Holý *et al.*, Phys. Rev. B **47**, 15 896 (1993).
[31] V. Holý and T. Baumbach, Phys. Rev. B **49**, 10 669 (1994).
[32] V. M. Kaganer, S. A. Stepanov, and R. Köhler, Phys. Rev. B **52**, 16 369 (1995).
[33] G. H. Vineyard, Phys. Rev. B **26**, 4146 (1982).
[34] H. Dosch, *Critical Phenomena at Surfaces and Interfaces (Evanescent X-Ray and Neutron Scattering)*, Springer Tracts in Modern Physics Vol. 126 (Springer-Verlag, Berlin, 1992).
[35] S. Dietrich and A. Haase, Phys. Rep. **260**, 1 (1995).
[36] R. W. James, in *Solid State Physics*, edited by H. Ehrenreich and D. Turnbull (Academic, New York, 1963), Vol. 15, p. 53.
[37] B. W. Batterman and H. Cole, Rev. Mod. Phys. **36**, 681 (1964).
[38] Z. G. Pinsker, *Dynamical Scattering of X-Rays in Crystals* (Springer-Verlag, Berlin, 1981).
[39] P. A. Aleksandrov, A. M. Afanas'ev, and S. A. Stepanov, Kristallografiya **29**, 197 (1984) [Sov. Phys. Crystallogr. **29**, 119 (1984)],
[40] S. Takagi, J. Phys. Soc. Jpn. **26**, 1239 (1969).
[41] T. Salditt, T. H. Metzger, and J. Peisl, Phys. Rev. Lett. **73**, 2228 (1994).
[42] M. Rauscher, T. Salditt, and H. Spohn, Phys. Rev. B **52**, 16 885 (1995).
[43] L. D. Landau and E. M. Lifshitz, *Statistical Physics* (Pergamon, Oxford, 1980), Pt. 1.
[44] Z. H. Ming *et al.*, Phys. Rev. B **47**, 16 373 (1993).
[45] Y. H. Phang, D. E. Savage, R. Kariotis, and M. G. Lagally, J. Appl. Phys. **74**, 3181 (1993).
[46] J. Daillant and O. Bélorgey, J. Chem. Phys. **97**, 5824 (1992).
[47] S. K. Sinha, J. Phys. (France) III **4**, 1543 (1994).
[48] A. L. Golovin, R. M. Imamov, and S. A. Stepanov, Acta Crystallogr. A **40**, 225 (1984).
[49] We refer to this scheme as a single-crystal one according to the classification given in Fig. 3, although different realizations may contain more crystals (e.g., monochromators).
[50] Y. Yoneda, Phys. Rev. **131**, 2010 (1963).
[51] T. Jach and M. J. Bedzyk, Phys. Rev. B **42**, 5399 (1990).
[52] T. Jach and M. J. Bedzyk, Acta Crystallogr. A **49**, 346 (1993).
[53] A. P. Ulyanenkov, S. A. Stepanov, U. Pietsch, and R. Köhler, J. Phys. D **28**, 2522 (1995).
[54] The (222) reflection is forbidden, and the higher harmonics are additionally suppressed due to their lower critical angle of specular reflection from the sample.
[55] A. M. Afanas'ev *et al.*, Fiz. Tverd. Tela (Leningrad) **27**, 2274 (1985) [Sov. Phys. Solid State **27**, 1365 (1985)].
[56] A. M. Afanas'ev *et al.*, Kristallografiya **31**, 1066 (1986) [Sov. Phys. Crystallogr. **31**, 630 (1986)].